

# Complex Magnetic Behavior in $\text{RuO}_2$ Thin Films: Strain, Surface Effects, and Altermagnetic Signatures

Mojtaba Alaei,<sup>1,2</sup> Nafise Rezaei,<sup>1</sup> Ilia Mikhailov,<sup>1</sup> Artem R. Oganov,<sup>1</sup> and Alireza Qaiumzadeh<sup>3</sup>

<sup>1</sup>*Materials Discovery Laboratory, Skolkovo Institute of Science and Technology,  
Bolshoy Boulevard 30, Building 1, Moscow 121205, Russia*

<sup>2</sup>*Department of Physics, Isfahan University of Technology, Isfahan 84156-83111, Iran*

<sup>3</sup>*Center for Quantum Spintronics, Department of Physics,  
Norwegian University of Science and Technology, NO-7491 Trondheim, Norway*

(Dated: February 18, 2026)

$\text{RuO}_2$  has been proposed as a prototypical metallic  $d$ -wave altermagnet, a Néel-ordered compensated antiferromagnetic state exhibiting nonrelativistic momentum-dependent spin splitting; yet, its magnetic ground state remains controversial both theoretically and experimentally. Using comprehensive first-principles calculations, we investigate  $\text{RuO}_2$  thin films with (110), (100), and (001) orientations, both freestanding and supported on a  $\text{TiO}_2$  substrate. We show that magnetism in  $\text{RuO}_2$  thin films is highly fragile, strongly influenced by strain, surface orientation, and atomic relaxation, while also being highly sensitive to the choice of the Brillouin-zone integration scheme. Although tensile strain induces finite magnetic moments, none of the studied systems stabilizes a compensated antiferromagnetic state; hence, an altermagnetic ground state cannot be achieved. Instead, the magnetic response is characterized by pronounced layer- and site-dependent variations and incomplete moment compensation, resembling a ferrimagnetic-like state. Our results reconcile conflicting theoretical and experimental reports and underscore the sensitivity of  $\text{RuO}_2$  magnetism to structural and methodological details.

## I. INTRODUCTION

Finding and reliably identifying the true magnetic ground state of quantum materials remains one of the central challenges in condensed-matter physics and materials science [1, 2]. This task is particularly demanding in itinerant transition-metal oxides, where competing exchange interactions, electron itinerancy, and structural distortions often place the system close to multiple nearly degenerate magnetic instabilities [3, 4]. Even subtle perturbations, such as epitaxial strain, reduced dimensionality, surface termination, or details of electronic-structure methodology, can tip the balance between nonmagnetic, ferro-, ferri-, and antiferromagnetic states. Establishing the genuine magnetic ground state is, therefore, not only a fundamental problem but also a prerequisite for designing functional materials for spin-based technologies, where transport, symmetry, and magnetic order are intimately intertwined.

Recently, antiferromagnetic (AFM) materials exhibiting nonrelativistic, momentum-dependent spin splitting have been identified as a symmetry-distinct class of antiferromagnets beyond conventional spin-degenerate AFM systems [5–13]. In these systems, the spin splitting originates not from spin-orbit coupling but from the spin space/point group symmetry, which allows for exchange-driven lifting of spin degeneracy while preserving zero net magnetization. The resulting momentum-dependent spin splitting is constrained by crystal symmetry and can be classified according to its angular-momentum character in the electronic band structure. In particular, unconventional collinear AFM materials with even-parity spin splitting of  $d$ -,  $g$ -, or  $i$ -wave symmetry, collectively termed altermagnets, retain fully compensated magnetic

moments in real space while exhibiting sign-changing spin polarization across the Brillouin zone [10, 11]. This symmetry-enforced structure of the spin splitting distinguishes it from conventional  $s$ -wave AFMs, in which combined inversion or parity and time-reversal symmetries protect spin degeneracy throughout momentum space.

Among these unconventional collinear AFMs, the  $d$ -wave class is particularly attractive because its symmetry allows for directional spin-polarized transport via the spin-splitter effect and spin splitting torque [14, 15]. Despite rapid progress in identifying candidate materials, many proposed altermagnets are insulating, which limits their immediate applicability in spin-transport devices. For practical applications, metallic or semiconducting systems are considerably more desirable, as they enable direct electrical control and detection of spin-polarized currents.  $\text{RuO}_2$  has been proposed as a prominent metallic candidate, with symmetry analysis predicting  $d$ -wave altermagnetic order. Early *ab initio* calculations [14, 16, 17] and some indirect quantum transport experimental observations [17–25] support this possibility. However, more recent high-resolution measurements, such as X-ray linear dichroism, nuclear magnetic resonance, spin-ARPES, and neutron diffraction; along with advanced first-principles studies, have challenged this picture, indicating that bulk  $\text{RuO}_2$  may, in fact, be nonmagnetic or, at most, extremely close to a magnetic [26–30]. This apparent contradiction has fueled an ongoing debate regarding the true magnetic ground state of  $\text{RuO}_2$  in bulk and thin films [31–43].

*Ab initio* methods based on density functional theory (DFT) are powerful tools for determining magnetic ground states. Standard DFT calculations without an on-site Hubbard  $U$  correction predict a nonmagnetic

ground state for bulk  $\text{RuO}_2$ , whereas DFT+ $U$  calculations with  $U$  values of  $U > 0.6$  eV stabilize an antiferromagnetic state [26, 35, 44]. Although the applicability of DFT+ $U$ , which effectively enhances the localization of Ru 4d electrons, may be questioned for a system with predominantly itinerant character, the fact that magnetism emerges already for relatively small  $U$  values indicates that  $\text{RuO}_2$  lies in close proximity to a magnetic instability. This pronounced sensitivity implies that its electronic and magnetic properties can be strongly influenced by external perturbations, including strain, symmetry breaking at surfaces and interfaces, and chemical doping [29, 44–47].

Recent experimental measurements have focused on the epitaxial growth of  $\text{RuO}_2$  thin films on  $\text{TiO}_2$  substrates, highlighting the importance of reduced dimensionality and substrate-induced effects on their magnetic properties. These developments underscore the need for a clear microscopic understanding of magnetism in  $\text{RuO}_2$  from first principles. Although several recent *ab initio* investigations have focused on the magnetism of  $\text{RuO}_2$  thin films [29, 48], significant gaps remain in our understanding of the detailed magnetic behavior of these systems.

In this study, we perform comprehensive DFT calculations to achieve a microscopic understanding of the magnetic behavior of  $\text{RuO}_2$  thin films with (110), (001), and (100) orientations, both under strain and in the strain-free limit. Furthermore, we investigate  $\text{RuO}_2/\text{TiO}_2$  thin-film heterostructures with the same crystallographic orientations in order to elucidate the role of epitaxial coupling and interface effects.

Since the (110) orientation is the most thermodynamically stable surface for both  $\text{TiO}_2$  and  $\text{RuO}_2$  [49, 50], our analysis places particular emphasis on this configuration. For this orientation, we systematically assess the influence of Brillouin-zone sampling, structural relaxation, induced magnetization, and competing magnetic ordering patterns in order to obtain a robust and quantitatively reliable determination of the magnetic ground state.

Our calculations demonstrate that  $\text{RuO}_2$  single crystals and thin films remain non-magnetic in the absence of external perturbations. Magnetic order may develop only within a few layers near the interface under tensile strain. Nevertheless, even under these conditions, the system does not realize a compensated antiferromagnetic phase, but instead adopts a ferrimagnetic-like state with a finite net magnetization.

## II. METHOD AND STRUCTURES

### A. *Ab initio* details

We performed nonrelativistic, *exttab initio* density functional theory (DFT) calculations using the Quantum ESPRESSO package [51–53]. The electron–ion interactions were described using the Standard Solid-State Pseudopotentials (SSSP) library, PBEsol Efficiency ver-

sion 1.3.0 [54]. For the exchange–correlation functional, we employed the PBEsol approximation [55], a revised form of the Perdew–Burke–Ernzerhof (PBE) generalized gradient approximation (GGA) that provides improved accuracy for the structural properties of solids and surfaces. A vacuum spacing of approximately 15 Å was introduced in all thin-film calculations to avoid spurious interactions between periodic images. Brillouin-zone integrations were performed using a uniform  $k$ -point grid corresponding to a reciprocal-space resolution of 0.10 Å<sup>−1</sup>. The thin-film structures were constructed using the CIF2Cell code [56], and the initial Quantum ESPRESSO input files were generated with the QE input generator [54]. The plane-wave kinetic energy cutoff was set to 40 Ry for the wave functions and 400 Ry for the charge density.

We investigate three  $\text{RuO}_2$  thin-film surface orientations: (110), (100), and (001), considered both as freestanding slabs and supported on  $\text{TiO}_2$  substrates (see Fig. 1). The  $\text{RuO}_2/\text{TiO}_2$  heterostructures are constructed using the experimental crystal structure of  $\text{TiO}_2$ . For the  $\text{RuO}_2(110)/\text{TiO}_2(110)$  system, recently studied experimentally, we examine  $\text{RuO}_2$  film thicknesses ranging from one to seven Ru atomic layers. For the freestanding  $\text{RuO}_2(110)$  thin film, a 17-layer Ru slab is employed to ensure convergence with respect to slab thickness and to minimize spurious interactions between the two surfaces. For the supported  $\text{RuO}_2(100)/\text{TiO}_2(100)$  and  $\text{RuO}_2(001)/\text{TiO}_2(001)$  heterostructures, the  $\text{RuO}_2$  film thickness is fixed at 12 Ru atomic layers. In the case of freestanding  $\text{RuO}_2(100)$  and  $\text{RuO}_2(001)$  thin films, thicker slabs consisting of 33 and 35 Ru atomic layers, respectively, are used to achieve well-converged surface properties.

The  $\text{RuO}_2/\text{TiO}_2$  heterostructure slabs were constructed by placing  $\text{RuO}_2$  layers symmetrically on both sides of the  $\text{TiO}_2$  substrate. This symmetric geometry avoids artificial effects associated with asymmetric slab models, where depositing  $\text{RuO}_2$  on only one side can introduce a net dipole moment across the slab. In such cases, spin-polarized calculations may yield spurious magnetic moments on the Ti atoms at the exposed surface. By eliminating the net dipole moment, the symmetric slab geometry suppresses these artifacts and ensures a physically meaningful description of the magnetic properties.

For the  $\text{RuO}_2(110)$  thin film, three distinct  $(1 \times 1)$  terminations of the rutile structure have been reported in the literature [57]. In this work, we consider two of these terminations. The relative stability of these terminations depends on the oxygen chemical potential, reflecting the oxygen availability during growth or operation [57]. Under oxygen-rich conditions, the stoichiometric  $\text{RuO}_2(110)-\text{O}^{\text{bridge}}$  termination is the most stable and is widely regarded as the preferred configuration of the rutile (110) surface. Under oxygen-poor conditions, the surface instead favors the  $\text{RuO}_2(110)-\text{O}^{\text{cus}}$  termination, characterized by coordinatively unsaturated Ru sites

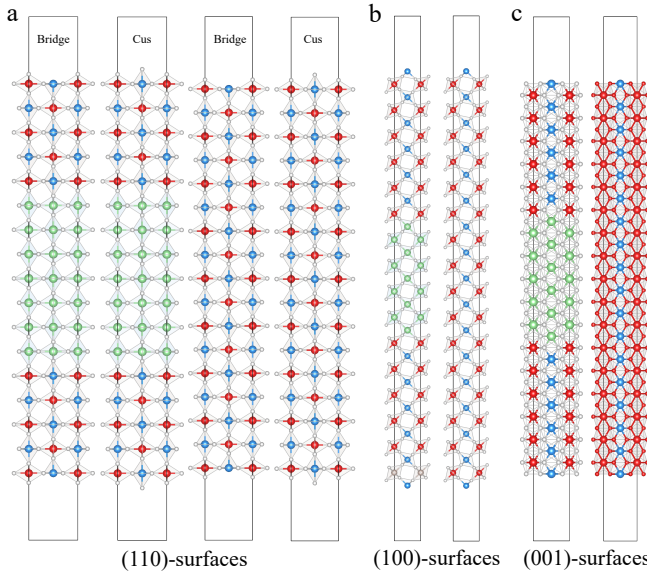


FIG. 1. Different surface orientations of  $\text{RuO}_2$  thin films considered in this work. For the  $\text{RuO}_2(110)/\text{TiO}_2(110)$  heterostructure, several film thicknesses were examined; the 5-L configuration is shown as a representative example. Blue and red spheres denote Ru atoms carrying different magnetic moments in the assumed AFM configurations discussed in the main text (labelled  $\text{Ru}_1$  and  $\text{Ru}_2$ ). Ti and O atoms are shown in green and white, respectively.

(*cus*). The third possible termination,  $\text{RuO}_2(110)-\text{Ru}$ , is not considered here, as it is unstable even under strongly oxygen-deficient conditions. The two terminations examined in this work are illustrated in Fig. 1.

Since our explicit comparison of oxygen-rich and oxygen-poor terminations for the (110) orientation reveals no significant changes in the magnetic ordering, we confine our analysis of the (100) and (001) thin films to terminations without oxygen atoms atop the Ru sites.

The  $\text{RuO}_2(110)$  orientation displays a repeating three-layer stacking sequence consisting of two oxygen-only layers and one mixed Ru–O layer. A similar three-layer periodicity is found for the  $\text{RuO}_2(100)$  orientation, composed of two oxygen-only layers and one ruthenium-only layer. In contrast, for the (001) orientation, each atomic layer contains both Ru and O atoms. To adopt a unified notation for slab thickness, we define the thickness solely by the number of Ru-containing layers. For example, for the (110) surface, with its sequence of two O layers followed by one mixed Ru–O layer, we use the notation 1-L, 2-L, ...,  $n$ -L instead of the conventional tri-layer notation (1-TL, 2-TL, ...,  $n$ -TL).

### III. RESULTS

#### A. Magnetism and $k$ -point sampling sensitivity

A recent study [44] examined the influence of strain on the magnetic properties of bulk  $\text{RuO}_2$ , demonstrating that lattice expansion stabilizes magnetic order—an effect that has also been reported in other materials [58]. Furthermore, Ref. [44] showed that the calculated magnetic moment in bulk  $\text{RuO}_2$  is highly sensitive to the choice of  $k$ -point sampling, exhibiting pronounced fluctuations that were attributed to the fragile and unconventional nature of magnetism in this compound.

Here, we show that a significant part of these fluctuations originates from the specific Brillouin-zone integration scheme employed. To substantiate this point, we compute the absolute magnetization of  $\text{RuO}_2$  using the lattice parameters and atomic positions of rutile  $\text{TiO}_2$ . This choice effectively applies a tensile strain to  $\text{RuO}_2$ , under which the system stabilizes in an AFM ground state.

We tested several Brillouin-zone integration schemes across different  $k$ -point meshes, including smearing-based approaches such as Marzari–Vanderbilt–DeVita–Payne cold smearing [59] and Fermi–Dirac smearing. Because smearing methods depend on the choice of the broadening parameter ( $\sigma$ ), we also employed the optimized tetrahedron method [60], which enables accurate Brillouin-zone integration without smearing. The resulting absolute magnetizations were then systematically compared across all integration schemes and  $k$ -point grids.

As shown in Fig. 2, the calculated magnetization is highly sensitive to both the choice of the smearing scheme and the value of the broadening parameter  $\sigma$ . For example, Fermi–Dirac smearing with  $\sigma = 0.01\text{--}0.03$  Ry yields a nearly vanishing magnetization, whereas cold smearing under the same conditions produces a large absolute magnetization of approximately  $1.0 \mu_B$ . These results underscore the importance of carefully selecting the Brillouin-zone integration scheme and broadening parameter when investigating magnetism in  $\text{RuO}_2$ .

In subsequent calculations, we performed structural relaxations using a small electronic broadening ( $\sigma = 0.00125$  Ry), which yields results nearly identical to those obtained with the optimized tetrahedron method. Final total-energy and magnetic-property calculations were then carried out using the optimized tetrahedron method to ensure an accurate treatment of Brillouin-zone integration.

#### B. $\text{RuO}_2(110)$ thin films on $\text{TiO}_2(110)$

Recent experimental investigations of the electronic band structure and transport properties of  $\text{RuO}_2$  have focused on  $\text{RuO}_2(110)$  thin films grown on  $\text{TiO}_2(110)$ , owing to their favorable epitaxial matching and structural stability. We first investigate  $\text{RuO}_2(110)$  thin films with

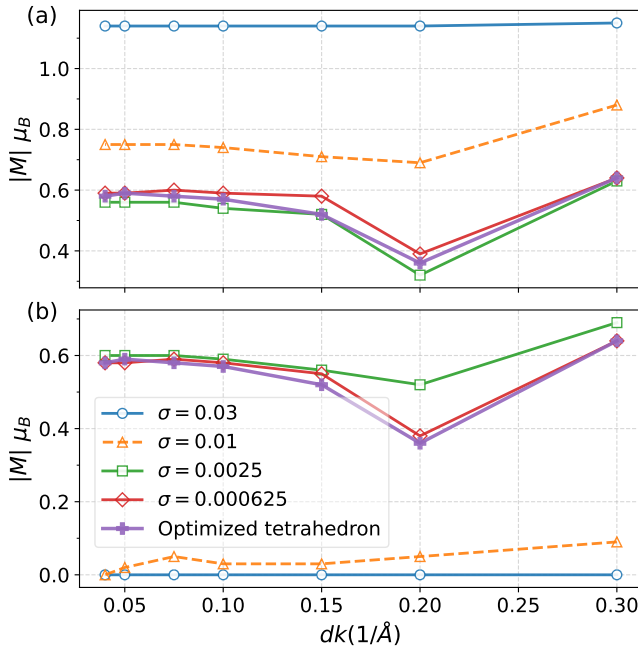


FIG. 2. Sensitivity of the Ru magnetic moment to  $k$ -point sampling in bulk rutile  $\text{RuO}_2$  under tensile strain. The calculations are performed for bulk  $\text{RuO}_2$  constructed using the lattice parameters and Wyckoff positions of rutile  $\text{TiO}_2$ , which leads to a tensile strain and stabilizes an AFM state.  $k$ -point densities range from  $0.05 \text{ \AA}^{-1}$  (corresponding to a  $27 \times 27 \times 42$  Monkhorst-Pack mesh) to  $0.30 \text{ \AA}^{-1}$  (corresponding to a  $5 \times 5 \times 8$  mesh). (a) Ru magnetic moment as a function of the Monkhorst-Pack  $k$ -point grid calculated using Marzari–Vanderbilt–DeVita–Payne cold smearing for different smearing widths  $\sigma$  (in Rydberg). Results obtained with the optimized tetrahedron method, which does not require a smearing parameter, are shown for comparison. (b) Same analysis performed using Fermi–Dirac smearing.

thicknesses ranging from one to seven Ru-containing layers grown on a  $\text{TiO}_2(110)$  substrate. Site-resolved magnetic moments are obtained by Bader partitioning of the spin density. In the AFM phase of bulk  $\text{RuO}_2$ , the rutile structure contains two inequivalent Ru sites that form distinct magnetic sublattices, which we label  $\text{Ru}_1$  and  $\text{Ru}_2$ . These sites are indicated in Fig. 1 by blue ( $\text{Ru}_1$ ) and red ( $\text{Ru}_2$ ) spheres.

Figure 3 presents the magnetic moments of  $\text{Ru}_1$  and  $\text{Ru}_2$  as a function of film thickness. In contrast to compensated AFM materials, the moments on  $\text{Ru}_1$  and  $\text{Ru}_2$  do not completely cancel. As a result, the  $\text{RuO}_2(110)$  thin film grown on a  $\text{TiO}_2(110)$  substrate develops a finite net magnetization, indicative of ferrimagnetic-like behavior.

Moreover, the magnetic moments exhibit a non-monotonic dependence on film thickness: the moments on both  $\text{Ru}_1$  and  $\text{Ru}_2$  oscillate as the number of Ru-containing layers increases, although without a strictly periodic pattern. These variations are most pronounced at the outermost surface layer and at the

$\text{RuO}_2/\text{TiO}_2(110)$  interface, underscoring the strong influence of surface and interface effects on the magnetic properties.

To further characterize the magnetic behavior of  $\text{RuO}_2(110)/\text{TiO}_2(110)$ , we examine three key factors: the influence of the initial magnetic configuration, the role of atomic relaxation, and the impact of induced magnetic moments.

Because standard DFT calculations cannot systematically sample the full magnetic energy landscape, the choice of the initial magnetic configuration is particularly important for  $\text{RuO}_2$ , where magnetic moments, if any, are intrinsically small. Exhaustive exploration of all possible magnetic initializations for different thicknesses is computationally prohibitive; we therefore perform a detailed analysis for a representative slab with a thickness of 3-L.

For this system, each layer contains two inequivalent Ru atoms ( $\text{Ru}_1$  and  $\text{Ru}_2$ ), yielding a total of six magnetic sites and ten distinct AFM configurations. We systematically examined all these AFM arrangements. Each configuration was initially imposed using magnetic constraints to stabilize the desired spin pattern; the constraints were subsequently released to allow full self-consistent relaxation. Among all tested configurations, the one initialized with antiparallel magnetic moments between  $\text{Ru}_1$  and  $\text{Ru}_2$  within each layer consistently relaxes to the lowest-energy state, characterized by opposite signs of the magnetic moments on  $\text{Ru}_1$  and  $\text{Ru}_2$ , with incomplete compensation. The remaining AFM initializations either converge to higher-energy solutions or evolve into this same configuration upon relaxation. Moreover, for several slab thicknesses, calculations starting from a ferromagnetic state also converge to this energetically favorable AFM ordering. These results indicate that the ground state generally favors antiparallel alignment between  $\text{Ru}_1$  and  $\text{Ru}_2$  within each layer; accordingly, this antiparallel arrangement is adopted as the initial magnetic configuration in all subsequent calculations.

The only deviation from this trend occurs in the 6-L slab, where the Ru atoms in the third layer develop magnetic moments of the same sign on the two sublattices, despite being initialized in the constrained AFM configuration. Nevertheless, the magnetization in this layer remains strongly uncompensated, since the moment on  $\text{Ru}_2$  is significantly smaller than that on  $\text{Ru}_1$ , resulting in a ferromagnetic alignment of the two sublattices, albeit with strongly unequal magnetic moments. The magnetic moments in the third layer are  $0.33 \mu\text{B}$  on  $\text{Ru}_1$  and  $0.04 \mu\text{B}$  on  $\text{Ru}_2$  for the bridge configuration, whereas for the cus configuration the corresponding values are  $0.30 \mu\text{B}$  and  $0.007 \mu\text{B}$ , respectively.

Although full structural relaxations were carried out for all slab geometries, Fig. 4 shows that atomic relaxation has only a minor effect on the magnetic moments of the deeper  $\text{RuO}_2(110)$  layers. Moreover, when the magnetic moment of the surface layer is artificially en-

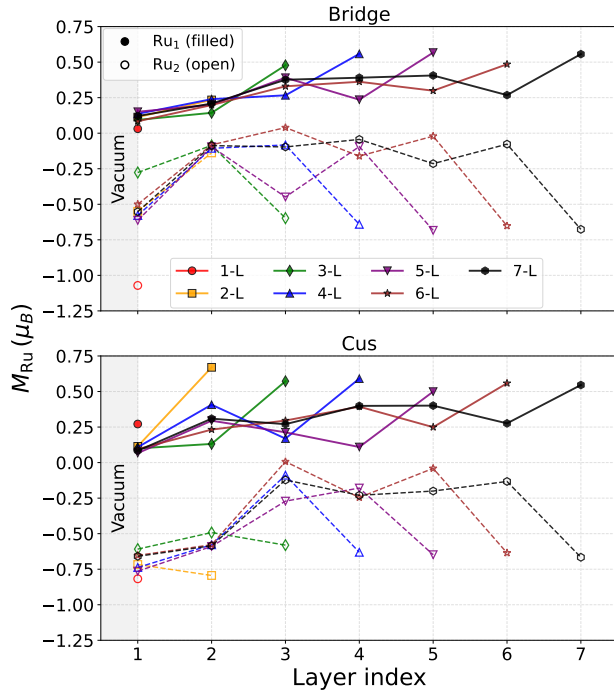


FIG. 3. Magnetic moments of  $\text{Ru}_1$  and  $\text{Ru}_2$  as a function of layer index and film thickness. Filled and open symbols denote  $\text{Ru}_1$  and  $\text{Ru}_2$ , respectively, for  $\text{RuO}_2(110)$  thin films on a  $\text{TiO}_2(110)$  substrate, with thicknesses ranging from 1-L to 7-L. For each thickness, magnetic moments are shown for all Ru layers within the slab. Data corresponding to the same film thickness are connected by lines of the same color to guide the eye.

hanced using a Hubbard  $U$  correction, the resulting increase remains highly localized: the magnetic moments in the subsurface and deeper layers change only negligibly. This behavior demonstrates that the magnetization generated at the surface due to symmetry breaking [29] does not propagate into the deeper layers. Instead, the magnetic moments of the Ru atoms are primarily determined by strain-induced changes in their local atomic environment arising from interfacial tensile strain, rather than by long-range induction from the surface.

It is also instructive to compare the electronic structure of a compensated AFM  $\text{RuO}_2(110)/\text{TiO}_2(110)$  thin film with that of its true magnetic ground state. To this end, we calculate and compare the band structures of a 5-L  $\text{RuO}_2(110)$  slab on a  $\text{TiO}_2(110)$  substrate for two cases: (i) a constrained, fully compensated AFM configuration, which hosts nonrelativistic altermagnetic spin-split bands, and (ii) the unconstrained AFM ground state. In both cases, the non-relaxed geometry is employed to avoid additional effects arising from structural relaxation.

To make the comparison between the two configurations meaningful, we adjusted the fixed magnetic moments of the Ru atoms in the constrained AFM case so

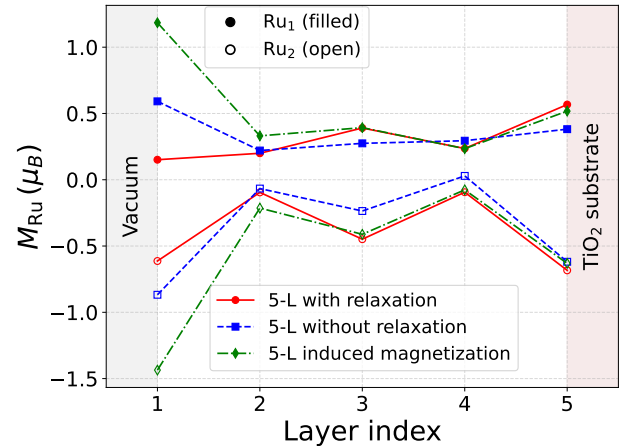


FIG. 4. Effect of atomic relaxation and induced magnetization on Ru magnetic moments in a 5-L  $\text{RuO}_2(110)$  slab on  $\text{TiO}_2(110)$ . Magnetic moments of  $\text{Ru}_1$  (filled symbols) and  $\text{Ru}_2$  (open symbols) are shown as a function of the Ru layer index.

that their total absolute magnetization matches that of the unconstrained AFM ground state, where the magnetic moments vary from layer to layer (Fig. 3). Here, the total absolute magnetization is defined as  $M_{\text{abs}} = \int_{\text{cell}} |n_{\text{up}}(\mathbf{r}) - n_{\text{down}}(\mathbf{r})| d^3r$ , where  $n_{\text{up}}(\mathbf{r})$  and  $n_{\text{down}}(\mathbf{r})$  are the spin-up and spin-down charge densities. By testing different values, we found that fixing the Ru moments to approximately  $0.3 \mu_B$  reproduces the total absolute magnetization of the unconstrained ground state. This value is therefore used in the constrained AFM calculation.

As shown in Fig. 5, the band structure of the magnetic ground state exhibits a substantially larger nonrelativistic spin splitting than that of the compensated AFM configuration. This enhancement arises because, in the true magnetic ground state, the Ru magnetic moments are not fully compensated, in contrast to the compensated AFM limit, where the net magnetization vanishes.

### C. $\text{RuO}_2(100)$ and $(001)$ thin films on $\text{TiO}_2(100)$ and $(001)$

We next consider the remaining low-index  $\text{RuO}_2$  surfaces, namely the (100) and (001) orientations. Owing to computational constraints, only one film thickness is examined for each case. For both orientations, we study a 12-layer  $\text{RuO}_2$  film grown on  $\text{TiO}_2$ . Figure 6 shows the layer-resolved magnetic moments of the two inequivalent Ru sites ( $\text{Ru}_1$  and  $\text{Ru}_2$ ), before and after structural relaxation.

For both surfaces, atomic relaxation has a markedly stronger effect than in the (110) case. In the relaxed (001) and (100) films, magnetic moments in the outermost three layers are strongly suppressed, while deeper

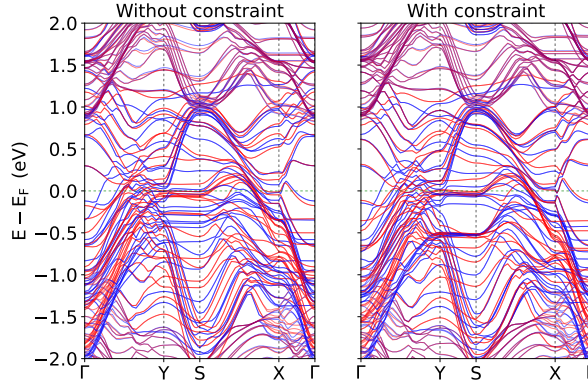


FIG. 5. Nonrelativistic band structures of a 5-L RuO<sub>2</sub>(110) slab on a TiO<sub>2</sub>(110) substrate. The left panel shows the band structure of the unconstrained magnetic ground state, while the right panel shows the band structure obtained with Ru magnetic moments constrained to enforce a fully compensated AFM configuration. In both cases, the non-relaxed atomic structure is used. Red and blue lines denote spin-up and spin-down bands, respectively.

layers near the RuO<sub>2</sub>/TiO<sub>2</sub> interface develop substantially larger local moments. By contrast, the unrelaxed films exhibit an almost ideal AFM arrangement, with Ru<sub>1</sub> and Ru<sub>2</sub> moments of similar magnitude and opposite sign; this ordering is significantly weakened upon relaxation.

Despite these differences, all systems, relaxed and unrelaxed, (001), (100), and (110), exhibit a characteristic layer-by-layer oscillation in the magnitude of the local magnetic moments. This behavior can be attributed to the metallic nature of the films: electronic states are confined between the surface–vacuum boundary and the buried interface, forming quasi-two-dimensional states analogous to a particle-in-a-box with finite potential barriers. The resulting quantum interference gives rise to oscillatory magnetic responses across the film thickness.

#### D. Intrinsic magnetism of freestanding RuO<sub>2</sub> thin films

To further explore the role of the substrate, we also study freestanding RuO<sub>2</sub> thin films with different surface orientations; see Fig. 1. Two classes of films are considered: (i) films constrained to the experimental lattice parameters of rutile TiO<sub>2</sub>, and (ii) films constrained to the experimental bulk lattice parameters of RuO<sub>2</sub>. In both cases, only the internal atomic coordinates are relaxed, while the lattice parameters are fixed. Since the in-plane rutile lattice constant of RuO<sub>2</sub> is approximately 0.1 Å larger than that of TiO<sub>2</sub>, constraining the film to the TiO<sub>2</sub> lattice imposes in-plane tensile strain. Therefore, adopting the TiO<sub>2</sub> lattice parameters provides an effective way to apply biaxial tensile strain to RuO<sub>2</sub> thin

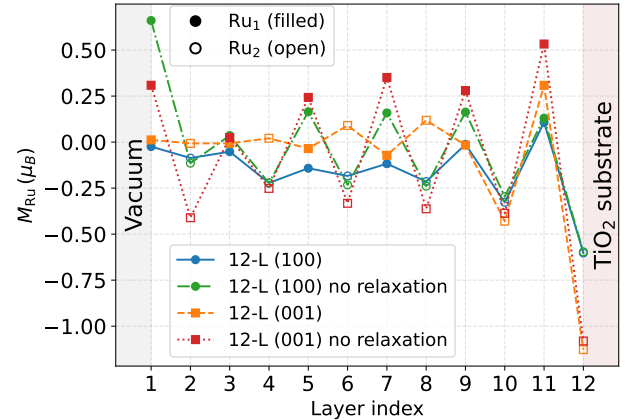


FIG. 6. Layer-resolved Ru magnetic moments for a 12-layer RuO<sub>2</sub> slab with (100) and (001) orientations on a TiO<sub>2</sub> substrate. Filled and open symbols denote Ru<sub>1</sub> and Ru<sub>2</sub> sites, respectively. Results are shown for both relaxed and unrelaxed atomic structures.

films.

Figure 7 shows the layer-resolved Ru magnetic moments for the (110), (100), and (001) orientations, both with and without tensile strain. In the unstrained (110) and (100) films, finite magnetic moments are largely confined to the first two surface layers and decay rapidly toward the bulk. The unstrained (110) result is consistent with recent reports (Ref. [29]).

In contrast, the (001) surface converges to a non-magnetic solution, with no Ru atom exhibiting a discernible magnetic moment. This finding differs from recent reports of finite magnetization at the (001) termination [48]. To evaluate the robustness of our results, we carried out additional calculations using VASP with several different PBE pseudopotentials for Ru, namely Ru, Ru\_pv, and Ru\_sv, corresponding to the valence configurations  $4d^75s^1$ ,  $4p^64d^75s^1$ , and  $4s^24p^64d^75s^1$ , respectively, as specified on the VASP website. All three yield the same outcome; for the unstrained (001) surface, the magnetic moments remain negligible ( $< 10^{-6} \mu_B$  per Ru atom). We therefore attribute the discrepancy to methodological differences, most likely related to the Brillouin-zone integration scheme, as our analysis indicates that the emergence of magnetism in RuO<sub>2</sub> is highly sensitive to the details of  $k$ -space sampling.

Under tensile strain, finite magnetization develops for all three surface orientations. However, the response of the (001) surface is markedly weaker: Ru atoms in the top layer carry moments of only  $\sim 0.02$ – $0.3 \mu_B$ , which decay rapidly in the subsurface layers. This indicates that the (001) thin film exhibits the weakest magnetic response even under tensile strain, rendering it the least favorable orientation among those studied for realizing antiferromagnetic behavior.

For RuO<sub>2</sub>(110) thin films, tensile strain qualitatively

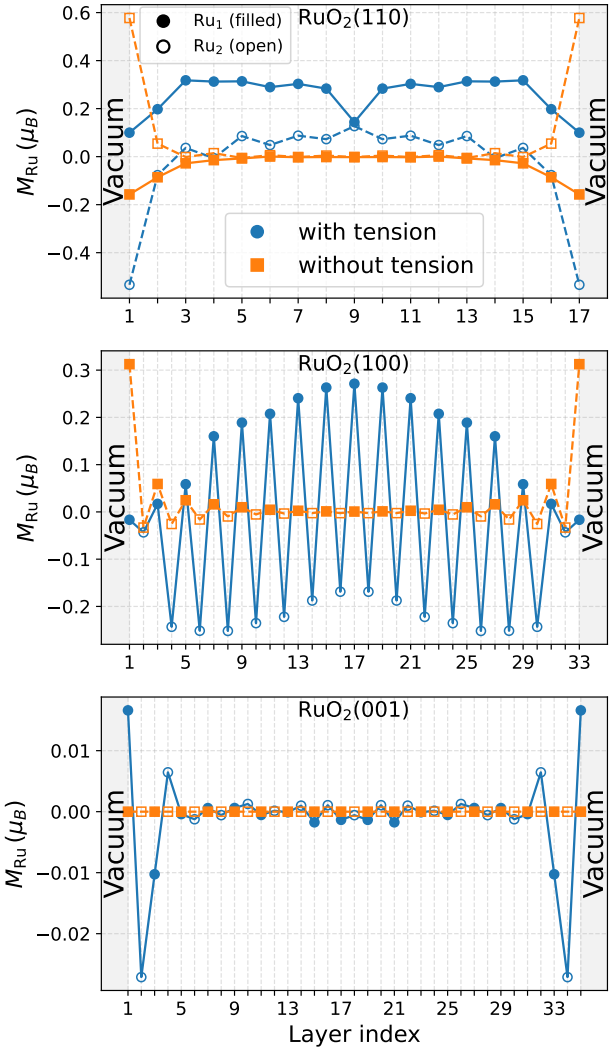


FIG. 7. Layer-resolved Ru magnetic moments for freestanding  $\text{RuO}_2$  slabs with (110), (100), and (001) orientations. For each orientation, two unrelaxed reference structures are shown: one constrained to the experimental  $\text{TiO}_2$  lattice parameters (tensile strain) and one using the experimental bulk  $\text{RuO}_2$  lattice. Filled and open symbols denote  $\text{Ru}_1$  and  $\text{Ru}_2$  sites, respectively.

alters the magnetic response relative to the unstrained case. In the topmost layers, the magnetic moments of the inequivalent Ru sites ( $\text{Ru}_1$  and  $\text{Ru}_2$ ) acquire opposite signs. Deeper in the slab, the  $\text{Ru}_1$  moment remains nearly constant at  $\sim 0.3 \mu\text{B}$ , whereas the  $\text{Ru}_2$  moment reverses sign and becomes small and positive ( $< 0.1 \mu\text{B}$ ). This pronounced layer- and site-dependent evolution underscores the complex strain-induced magnetism of the (110) surface.

For  $\text{RuO}_2(100)$  thin films, tensile strain induces the strongest tendency toward AFM alignment among the orientations studied; however, the system remains far from a fully compensated state. Our DFT calculations

yield a sizable net magnetic moment of approximately  $4.63 \mu\text{B}$  per unit cell, in contrast to recent reports [45] that propose the (100) orientation as an ideal altermagnet and the (110) surface as ferrimagnetic. Based on our analysis, none of the investigated surfaces, (110), (100), or (001), stabilize a compensated AFM and hence an altermagnetic ground state.

#### IV. SUMMARY AND CONCLUSION

In this work, we have performed a comprehensive first-principles investigation of the magnetic properties of  $\text{RuO}_2$  thin films with (110), (100), and (001) orientations, both as freestanding slabs and in  $\text{RuO}_2/\text{TiO}_2$  heterostructures. Motivated by the ongoing debate on the existence of  $d$ -wave altermagnetism in metallic  $\text{RuO}_2$ , we systematically examined the role of epitaxial strain, surface termination, film thickness, structural relaxation, and Brillouin-zone integration schemes in determining the magnetic ground state.

Our calculations demonstrate that magnetism in  $\text{RuO}_2$  thin films is intrinsically fragile and highly sensitive to both structural and methodological details. In particular, we show that the calculated magnetic moments depend strongly on the choice of Brillouin-zone integration scheme and smearing parameters. When treated with sufficiently accurate integration, bulk  $\text{RuO}_2$  at its experimental lattice parameters remains nonmagnetic, consistent with several recent experimental reports that question robust long-range antiferromagnetism in this compound. This sensitivity places  $\text{RuO}_2$  in close proximity to a magnetic instability, where small perturbations can induce local moments.

Epitaxial tensile strain, mimicked by constraining  $\text{RuO}_2$  to the rutile  $\text{TiO}_2$  lattice parameters, induces finite Ru magnetic moments for all investigated surface orientations. However, in no case do we find stabilization of a fully compensated Néel-ordered AFM state and hence any altermagnetic behavior. Instead, the magnetic response is strongly layer- and site-dependent, with incomplete compensation between the two Ru sublattices ( $\text{Ru}_1$  and  $\text{Ru}_2$ ). In  $\text{RuO}_2(110)/\text{TiO}_2(110)$  heterostructures, the magnetization is dominated by surface and interface layers and exhibits pronounced oscillations with film thickness, consistent with quantum confinement and modified Ru–O hybridization at the boundaries. Even when initialized in various magnetic configurations, the system relaxes to states characterized by residual net magnetization, i.e., ferrimagnetic-like order rather than a symmetry-protected compensated AFM state.

For freestanding films, unstrained (110) and (100) slabs develop only weak surface-localized moments, while the unstrained (001) surface remains essentially nonmagnetic within numerical accuracy. Under tensile strain, all orientations develop enhanced magnetization, but the compensation between  $\text{Ru}_1$  and  $\text{Ru}_2$  moments remains incomplete. Notably, the (100) orientation exhibits the

largest net magnetic moment under strain, yet still fails to realize a compensated altermagnetic phase. The (001) orientation shows the weakest magnetic response overall, even under tensile strain, making it the least favorable candidate for altermagnetic behavior among the studied surfaces.

By explicitly comparing the band structures of constrained compensated AFM configurations with those of the true magnetic ground states, we show that the larger nonrelativistic spin splitting observed in thin films originates from uncompensated magnetization rather than from a symmetry-enforced altermagnetic state. Therefore, any experimentally observed spin splitting or anomalous transport in RuO<sub>2</sub> thin films must be carefully interpreted in light of possible ferrimagnetic-like surface or interface contributions, rather than being directly attributed to ideal *d*-wave altermagnetism.

Overall, our results reconcile seemingly conflicting theoretical and experimental findings by demonstrating that RuO<sub>2</sub> resides at the brink of magnetism: small strain, reduced dimensionality, or methodological differences can induce local magnetic moments; yet none of the studied realistic thin-film geometries stabilize a fully compensated altermagnetic ground state. These findings underscore the importance of rigorous numerical conver-

gence and detailed structural modeling when identifying candidate altermagnets, and they suggest that achieving robust altermagnetism in RuO<sub>2</sub> may require additional symmetry engineering, chemical modification, or external tuning beyond simple epitaxial strain.

In addition, our findings call for a careful re-evaluation of recent anomalous Hall measurements in RuO<sub>2</sub> thin films that have been interpreted within a fully compensated altermagnetic framework. Since our calculations reveal an unconventional ferrimagnetic-like order with finite net magnetization in strained and heterostructured geometries, conventional Berry-curvature-driven anomalous Hall contributions are expected. These epitaxial thin films grown on TiO<sub>2</sub> can also host strong spin-orbit couplings. We therefore propose systematic thickness- and strain-dependent transport measurements to distinguish genuine symmetry-enforced altermagnetism from the unusual uncompensated magnetism predicted in this work.

## ACKNOWLEDGMENTS

A.Q. has been supported by the Research Council of Norway through its Centers of Excellence funding scheme, Project No. 262633 “QuSpin” and FRIPRO with Project No. 353919 “QTransMag.”

---

[1] A. Tellez-Mora, X. He, E. Bousquet, L. Wirtz, and A. H. Romero, Systematic determination of a material’s magnetic ground state from first principles, *npj Comput. Mater.* **10**, 20 (2024).

[2] J. G. Aldea, D. L. Esteras, S. Roche, and J. H. Garcia, Challenges and strategies for first-principles simulations of two-dimensional magnetic phenomena, *Nanoscale* **17**, 24955 (2025).

[3] J. B. Goodenough, Perspective on engineering transition-metal oxides, *Chem. Mater.* **26**, 820 (2014).

[4] I. V. Solovyev, *Magnetic interactions in transition-metal oxides* (2003), arXiv:cond-mat/0305668 [cond-mat.mtrl-sci].

[5] Y. Noda, K. Ohno, and S. Nakamura, Momentum-dependent band spin splitting in semiconducting MnO<sub>2</sub>: a density functional calculation, *Phys. Chem. Chem. Phys.* **18**, 13294 (2016).

[6] S. Hayami, Y. Yanagi, and H. Kusunose, Momentum-dependent spin splitting by collinear antiferromagnetic ordering, *J. Phys. Soc. Jpn.* **88**, 123702 (2019).

[7] M. Naka, S. Hayami, H. Kusunose, Y. Yanagi, Y. Motome, and H. Seo, Spin current generation in organic antiferromagnets, *Nat. Commun.* **10**, 4305 (2019).

[8] L.-D. Yuan, Z. Wang, J.-W. Luo, E. I. Rashba, and A. Zunger, Giant momentum-dependent spin splitting in centrosymmetric low-*Z* antiferromagnets, *Phys. Rev. B* **102**, 014422 (2020).

[9] L. Šmejkal, R. González-Hernández, T. Jungwirth, and J. Sinova, Crystal time-reversal symmetry breaking and spontaneous Hall effect in collinear antiferromagnets, *Sci. Adv.* **6**, eaaz8809 (2020).

[10] L. Šmejkal, J. Sinova, and T. Jungwirth, Emerging Research Landscape of Altermagnetism, *Phys. Rev. X* **12**, 040501 (2022).

[11] L. Šmejkal, A. B. Hellenes, R. González-Hernández, J. Sinova, and T. Jungwirth, Giant and Tunneling Magnetoresistance in Unconventional Collinear Antiferromagnets with Nonrelativistic Spin-Momentum Coupling, *Phys. Rev. X* **12**, 011028 (2022).

[12] J. Krempaský, L. Šmejkal, S. D’souza, M. Hajlaoui, G. Springholz, K. Uhlířová, F. Alarab, P. Constantinou, V. Strocov, D. Usanov, *et al.*, Altermagnetic lifting of Kramers spin degeneracy, *Nature* **626**, 517 (2024).

[13] M. Alaei, P. Sobieszczyk, A. Ptok, N. Rezaei, A. R. Oganov, and A. Qaiumzadeh, Origin of *A*-type antiferromagnetism and chiral split magnons in altermagnetic  $\alpha$ -MnTe, *Phys. Rev. B* **111**, 104416 (2025).

[14] R. González-Hernández, L. Šmejkal, K. Výborný, Y. Yaghagi, J. Sinova, T. Jungwirth, and J. Železný, Efficient Electrical Spin Splitter Based on Nonrelativistic Collinear Antiferromagnetism, *Phys. Rev. Lett.* **126**, 127701 (2021).

[15] E. W. Hodt, A. Qaiumzadeh, and J. Linder, Phonon-enhanced optical spin conductivity and spin-splitter effect in altermagnets, *Phys. Rev. B* **113**, 054403 (2026).

[16] L. Šmejkal, A. Marmodoro, K.-H. Ahn, R. González-Hernández, I. Turek, S. Mankovsky, H. Ebert, S. W. D’Souza, O. c. v. Šipr, J. Sinova, and T. c. v. Jungwirth, Chiral Magnons in Altermagnetic RuO<sub>2</sub>, *Phys. Rev. Lett.* **131**, 256703 (2023).

[17] O. Fedchenko, J. Minár, A. Akashdeep, S. W. D’Souza, D. Vasilyev, O. Tkach, L. Odenbreit, Q. Nguyen, D. Kut

nyakov, N. Wind, L. Wenthaus, M. Scholz, K. Rossnagel, M. Hoesch, M. Aeschlimann, B. Stadtmüller, M. Kläui, G. Schönhense, T. Jungwirth, A. B. Hellenes, G. Jakob, L. Šmejkal, J. Sinova, and H.-J. Elmers, Observation of time-reversal symmetry breaking in the band structure of altermagnetic RuO<sub>2</sub>, *Sci. Adv.* **10**, eadj4883 (2024).

[18] J. Song, S. H. Lee, S. Kang, D. Kim, J. H. Jeong, T. Oh, S. Lee, S. Lee, K.-H. Ahn, K.-W. Lee, M. Kim, T. W. Noh, B.-J. Yang, and C. Kim, Spin-Orbit Coupling Driven Magnetic Response in Altermagnetic RuO<sub>2</sub>, *Small* **21**, 2407722 (2025).

[19] Z. Feng, X. Zhou, L. Šmejkal, L. Wu, Z. Zhu, H. Guo, R. González-Hernández, X. Wang, H. Yan, P. Qin, *et al.*, An anomalous hall effect in altermagnetic ruthenium dioxide, *Nat. Electron.* **5**, 735 (2022).

[20] C. He, Z. Wen, J. Okabayashi, Y. Miura, T. Ma, T. Ohkubo, T. Seki, H. Sukegawa, and S. Mitani, Evidence for single variant in altermagnetic RuO<sub>2</sub>(101) thin films, *Nat. Commun.* **16**, 8235 (2025).

[21] Y. Kobayashi, S. Karube, I. Sugiura, H. Narita, R. Hisatomi, Y. Shiota, and T. Ono, Detection of an-  
tiferromagnetic order in a RuO<sub>2</sub>/Pt bilayer by spin Hall magnetoresistance, *AIP Advances* **14**, 115120 (2024).

[22] Y. Zhang, H. Bai, J. Dai, L. Han, C. Chen, S. Liang, Y. Cao, Y. Zhang, Q. Wang, W. Zhu, F. Pan, and C. Song, Electrical manipulation of spin splitting torque in altermagnetic RuO<sub>2</sub>, *Nat. Commun.* **16**, 5646 (2025).

[23] S. G. Jeong, I. H. Choi, S. Nair, L. Buiarelli, B. Pourbahari, J. Y. Oh, N. Bassim, D. Hirai, A. Seo, W. S. Choi, R. M. Fernandes, T. Birol, L. Zhao, J. S. Lee, and B. Jalan, *Altermagnetic Polar Metallic phase in Ultra-Thin Epitaxially-Strained RuO<sub>2</sub> Films* (2025), arXiv:2405.05838 [cond-mat.mtrl-sci].

[24] S. G. Jeong, S. Lee, B. Lin, Z. Yang, I. H. Choi, J. Y. Oh, S. Song, S. W. Lee, S. Nair, R. Choudhary, J. Parikh, S. Park, W. S. Choi, J. S. Lee, J. M. LeBeau, T. Low, and B. Jalan, Metallicity and anomalous Hall effect in epitaxially strained, atomically thin RuO<sub>2</sub> films, *Proc. Natl. Acad. Sci. U.S.A.* **122**, e2500831122 (2025).

[25] A. J. Howzen, S. Gupta, G. Burnell, and N. Satchell, *Transport spin polarization in RuO<sub>2</sub> films* (2026), arXiv:2601.19052 [cond-mat.mes-hall].

[26] A. Smolyanyuk, I. I. Mazin, L. Garcia-Gassull, and R. Valentí, Fragility of the magnetic order in the prototypical altermagnet RuO<sub>2</sub>, *Phys. Rev. B* **109**, 134424 (2024).

[27] D. T. Plouff, L. Scheuer, S. Shrestha, W. Wu, N. J. Parvez, S. Bhatt, X. Wang, L. Gundlach, M. B. Jungfleisch, and J. Q. Xiao, Revisiting altermagnetism in RuO<sub>2</sub>: a study of laser-pulse induced charge dynamics by time-domain terahertz spectroscopy, *npj Spintronics* **3**, 17 (2025).

[28] T. Osumi, K. Yamauchi, S. Souma, S. Paul, A. Honma, K. Nakayama, K. Ozawa, M. Kitamura, K. Horiba, H. Kumigashira, C. Bigi, F. m. c. Bertran, T. Oguchi, T. Takahashi, Y. Maeno, and T. Sato, Spin-degenerate bulk bands and topological surface states associated with Dirac nodal lines in RuO<sub>2</sub>, *Phys. Rev. B* **113**, 085116 (2026).

[29] D. Q. Ho, D. Q. To, R. Hu, G. W. Bryant, and A. Janotti, Symmetry-breaking induced surface magnetization in nonmagnetic RuO<sub>2</sub>, *Phys. Rev. Mater.* **9**, 094406 (2025).

[30] S. Wang, C. Wang, Y. Yuan, J. Li, F. Pei, D. Liu, C. Qin, J. Cao, Y. Wang, T. Wang, J. Liu, J.-E. Lee, G. Zhang, C. Klewe, C. Yu, F. Zhang, D. Song, K. Chen, W. Zhao, D. Shen, Z. Qiu, M. Yang, B. Hong, and Q. Li, Absence of magnetic order in epitaxial RuO<sub>2</sub> revealed by x-ray linear dichroism, *Phys. Rev. B* **113**, 024439 (2026).

[31] I. H. Choi, S. G. Jeong, B. Jalan, and J. S. Lee, Exploring altermagnetism in RuO<sub>2</sub>: from conflicting experiments to emerging consensus, *Nano Convergence* **13**, 1 (2026).

[32] S. G. Jeong, S. Lee, J. Y. Oh, B. Y. X. Lin, A. Santosh, J. M. LeBeau, A. J. Grutter, W. S. Choi, T. Low, V. Lauter, and B. Jalan, *Emergence of unconventional magnetic order in strain-engineered RuO<sub>2</sub>/TiO<sub>2</sub> superlattices* (2026), arXiv:2601.10518 [cond-mat.mtrl-sci].

[33] J. Liu, J. Zhan, T. Li, J. Liu, S. Cheng, Y. Shi, L. Deng, M. Zhang, C. Li, J. Ding, Q. Jiang, M. Ye, Z. Liu, Z. Jiang, S. Wang, Q. Li, Y. Xie, Y. Wang, S. Qiao, J. Wen, Y. Sun, and D. Shen, Absence of Altermagnetic Spin Splitting Character in Rutile Oxide RuO<sub>2</sub>, *Phys. Rev. Lett.* **133**, 176401 (2024).

[34] J. Song, C. Mu, S. Zhu, X. Zhou, W. Wu, Y.-z. Long, J. Luo, and Z. Li, Absence of magnetic order and magnetic fluctuations in RuO<sub>2</sub>, *Phys. Rev. B* **112**, 144444 (2025).

[35] P. Keßler, L. Garcia-Gassull, A. Suter, T. Prokscha, Z. Salman, D. Khalyavin, P. Manuel, F. Orlandi, I. I. Mazin, R. Valentí, *et al.*, Absence of magnetic order in RuO<sub>2</sub>: insights from  $\mu$  sr spectroscopy and neutron diffraction, *npj Spintronics* **2**, 50 (2024).

[36] M. Hiraishi, H. Okabe, A. Koda, R. Kadono, T. Muroi, D. Hirai, and Z. Hiroi, Nonmagnetic Ground State in RuO<sub>2</sub> Revealed by Muon Spin Rotation, *Phys. Rev. Lett.* **132**, 166702 (2024).

[37] M. Wenzel, E. Uykur, S. Rößler, M. Schmidt, O. Janson, A. Tiwari, M. Dressel, and A. A. Tsirlin, Fermi-liquid behavior of nonaltermagnetic RuO<sub>2</sub>, *Phys. Rev. B* **111**, L041115 (2025).

[38] X. Peng, Z. Liu, S. Zhang, Y. Zhou, Y. Sun, Y. Su, C. Wu, T. Zhou, L. Liu, Y. Li, *et al.*, Universal scaling behavior of transport properties in non-magnetic RuO<sub>2</sub>, *Commun. Mater.* **6**, 177 (2025).

[39] Y.-X. Li, Y. Chen, L. Pan, S. Li, S.-B. Zhang, and H.-Z. Lu, *Exploration of altermagnetism in RuO<sub>2</sub>* (2026), arXiv:2509.19932 [cond-mat.mes-hall].

[40] A. Akashdeep, S. Krishnia, J.-H. Ha, S. An, M. Gaerner, T. Prokscha, A. Suter, G. Janka, G. Reiss, T. Kuschel, D.-S. Han, A. Di Bernardo, Z. Salman, G. Jakob, and M. Kläui, Surface-localized magnetic order in RuO<sub>2</sub> thin films revealed by low-energy muon probes, *Appl. Phys. Lett.* **128**, 022406 (2026).

[41] H. Chen, Z.-A. Wang, P. Qin, Z. Meng, X. Zhou, X. Wang, L. Liu, G. Zhao, Z. Duan, T. Zhang, J. Liu, D.-F. Shao, C. Jiang, and Z. Liu, Spin-Splitting Magnetoresistance in Altermagnetic RuO<sub>2</sub> Thin Films, *Adv. Mater.* **37**, 2507764 (2025).

[42] Z. Lin, D. Chen, W. Lu, X. Liang, S. Feng, K. Yamagami, J. Osiecki, M. Leandersson, B. Thiagarajan, J. Liu, C. Felser, and J. Ma, Bulk band structure of RuO<sub>2</sub> measured with soft x-ray angle-resolved photoemission spectroscopy, *Phys. Rev. B* **111**, 134450 (2025).

[43] S. Lee, S. G. Jeong, J.-P. Wang, B. Jalan, and T. Low, *Strain-Driven Altermagnetic Spin Splitting Effect in RuO<sub>2</sub>* (2026), arXiv:2602.11602 [cond-mat.mtrl-sci].

[44] Z. Qian, Y. Yang, S. Liu, and C. Wu, Fragile unconventional magnetism in RuO<sub>2</sub> by proximity to Landau-Pomeranchuk instability, *Phys. Rev. B* **111**, 174425 (2025).

[45] J. D. Forte, S. G. Jeong, A. Santhosh, S. Lee, B. Jalan, and T. Low, Strain Engineering of Altermagnetic Symmetry in Epitaxial RuO<sub>2</sub> Films, arXiv preprint arXiv:2510.26581 <https://doi.org/10.48550/arXiv.2510.26581> (2025).

[46] D. Wickramaratne, M. Currie, S. S. Fields, C. D. Cress, and S. P. Bennett, Effects of altermagnetic order, strain, and doping in RuO<sub>2</sub>, *J. Mater. Chem. C* , (2026).

[47] E. Torun, C. M. Fang, G. A. de Wijs, and R. A. de Groot, Role of Magnetism in Catalysis: RuO<sub>2</sub> (110) Surface, *J. Phys. Chem. C* **117**, 6353 (2013).

[48] S. Brahimi, D. Prakash Rai, and S. Lounis, Confinement-induced altermagnetism in RuO<sub>2</sub> ultrathin films, *J. Phys. Condens. Matter* **37**, 395801 (2025).

[49] U. Diebold, The surface science of titanium dioxide, *Surf. Sci. Rep.* **48**, 53 (2003).

[50] H. A. Zakaryan, A. G. Kvashnin, and A. R. Oganov, Stable reconstruction of the (110) surface and its role in pseudocapacitance of rutile-like RuO<sub>2</sub>, *Sci. Rep.* **7**, 10357 (2017).

[51] P. Giannozzi, S. Baroni, N. Bonini, M. Calandra, R. Car, C. Cavazzoni, D. Ceresoli, G. L. Chiarotti, M. Cococcioni, I. Dabo, A. Dal Corso, S. de Gironcoli, S. Fabris, G. Fratesi, R. Gebauer, U. Gerstmann, C. Gougauss, A. Kokalj, M. Lazzeri, L. Martin-Samos, N. Marzari, F. Mauri, R. Mazzarello, S. Paolini, A. Pasquarello, L. Paulatto, C. Sbraccia, S. Scandolo, G. Sclauzero, A. P. Seitsonen, A. Smogunov, P. Umari, and R. M. Wentzcovitch, QUANTUM ESPRESSO: a modular and open-source software project for quantum simulations of materials, *J. Phys. Condens. Matter* **21**, 395502 (19pp) (2009).

[52] P. Giannozzi, O. Andreussi, T. Brumme, O. Bunau, M. B. Nardelli, M. Calandra, R. Car, C. Cavazzoni, D. Ceresoli, M. Cococcioni, N. Colonna, I. Carnimeo, A. D. Corso, S. de Gironcoli, P. Delugas, R. A. D. Jr, A. Ferretti, A. Floris, G. Fratesi, G. Fugallo, R. Gebauer, U. Gerstmann, F. Giustino, T. Gorni, J. Jia, M. Kawamura, H.-Y. Ko, A. Kokalj, E. Küçükbenli, M. Lazzeri, M. Marsili, N. Marzari, F. Mauri, N. L. Nguyen, H.-V. Nguyen, A. O. de-la Roza, L. Paulatto, S. Poncé, D. Rocca, R. Sabatini, B. Santra, M. Schlipf, A. P. Seitsonen, A. Smogunov, I. Timrov, T. Thonhauser, P. Umari, N. Vast, X. Wu, and S. Baroni, Advanced capabilities for materials modelling with QUANTUM ESPRESSO, *J. Phys. Condens. Matter* **29**, 465901 (2017).

[53] P. Giannozzi, O. Baseggio, P. Bonfà, D. Brunato, R. Car, I. Carnimeo, C. Cavazzoni, S. de Gironcoli, P. Delugas, F. Ferrari Ruffino, A. Ferretti, N. Marzari, I. Timrov, A. Urru, and S. Baroni, Quantum ESPRESSO toward the exascale, *J. Chem. Phys.* **152**, 154105 (2020).

[54] G. Prandini, A. Marrazzo, I. E. Castelli, N. Mounet, and N. Marzari, Precision and efficiency in solid-state pseudopotential calculations, *npj Comput. Mater.* **4**, 72 (2018), <http://materialscloud.org/sssp>.

[55] J. P. Perdew, A. Ruzsinszky, G. I. Csonka, O. A. Vydrov, G. E. Scuseria, L. A. Constantin, X. Zhou, and K. Burke, Restoring the Density-Gradient Expansion for Exchange in Solids and Surfaces, *Phys. Rev. Lett.* **100**, 136406 (2008).

[56] T. Björkman, CIF2Cell: Generating geometries for electronic structure programs, *Comput. Phys. Commun.* **182**, 1183 (2011).

[57] K. Reuter and M. Scheffler, Composition, structure, and stability of RuO<sub>2</sub>(110) as a function of oxygen pressure, *Phys. Rev. B* **65**, 035406 (2001).

[58] W. Zhang, M. Zheng, Y. Liu, Z. Zhang, R. Xiong, and Z. Lu, Strain-induced nonrelativistic altermagnetic spin splitting effect, *Phys. Rev. B* **112**, 024415 (2025).

[59] N. Marzari, D. Vanderbilt, A. De Vita, and M. C. Payne, Thermal Contraction and Disordering of the Al(110) Surface, *Phys. Rev. Lett.* **82**, 3296 (1999).

[60] M. Kawamura, Y. Gohda, and S. Tsuneyuki, Improved tetrahedron method for the Brillouin-zone integration applicable to response functions, *Phys. Rev. B* **89**, 094515 (2014).